ACS NANO
Cite This: ACS Nano 2019, 13, 14437−14446
www.acsnano.org

ARTICLE

Probing Multiphased Transition in Bulk MoS_2 by Direct Electron Injection

Krishna P. Dhakal,[§,#] Ganesh Ghimire,[§,#] Kyungwha Chung,[§,#] Dinh Loc Duong,[*,†,§] Sung Wng Kim,[*,§] and Jeongyong Kim[*,§]

[§]Department of Energy Science, Sungkyunkwan University, Suwon 16419, Republic of Korea
[†]Center for Integrated Nanostructure Physics, Institute for Basic Science, Suwon 16419, Republic of Korea

Supporting Information

ABSTRACT: **Structural phase transitions in layered two-dimensional (2D) materials are of significant interest owing to their ability to exist in multiple metastable states with distinctive properties. However, phase transition in bulk MoS_2 by nondestructive electron infusion has not yet been realized. In this study, we report the 2H to 1T′ phase transition and in-between intermediates in bulk MoS_2 using $MoS_2/[Ca_2N]^+\cdot e^-$ heterostructures, in which kinetic free electrons were directly injected into MoS_2. We observed various phases in MoS_2 ranging from heavily doped 2H to a distorted lattice state and then on to a complete 1T′ state. Snapshots of the multiphase transition were captured by extraordinary Raman shift and bandgap reduction and were further elucidated by theoretical calculations. We also observed a weakening in interlayer coupling in the vicinity of the metallic regime, which led to an unusually strong photoluminescence emission, suggesting light-efficient bulk MoS_2. Our results thus suggest the optoelectronic applications that can fully utilize the multiphase transition of bulk 2D materials.**

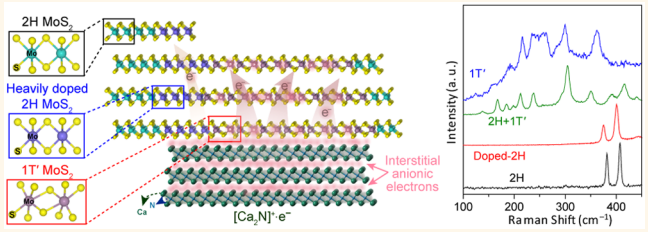

KEYWORDS: *MoS_2, $[Ca_2N]^+\cdot e^-$, electron injection, multiphase transition, interlayer weakening*

Two-dimensional (2D) semiconducting subset of transition-metal dichalcogenide (TMD) crystals, such as molybdenum disulfide (MoS_2), exist in a layered crystal structure in which the S atoms of each monolayer exist in the trigonal prismatic coordination pattern around Mo atoms with a hexagonal (2H) phase atomic stacking sequence.[1−8] MoS_2 exhibits an indirect bandgap (1.1 eV) in the bulk state but becomes a direct bandgap (1.9 eV) semiconductor in the monolayer state with a signature of strong photoluminescence (PL). Electronic structures of TMDs with interlayer coupling and inversion symmetry that varies with the number of layers enable diverse electronic and optoelectronic applications for MoS_2.[3−10] Recently, a method to switch between the metallic and insulating phases of semiconductors has been proposed for group VI-TMDs, such as MoS_2 and WS_2 crystals. Their metallic (1T′) phases exhibit a low contact resistance for field-effect transistors,[10] Weyl semimetals,[11] a quantum spin Hall effect,[12] and strong optical Kerr nonlinearity.[13] Among Mo-and W-based S, Se, and Te TMDs, metal sulfides (MS_2) exhibit the largest phase-transition energy (0.55 eV for MoS_2) between the 2H and 1T′ phases, while MTe_2 exhibits an order of low phase-transition energy (0.06 eV),[9] which indicates that it is a challenge to produce a metallic MS_2. Previously, several methods had been established to obtain the polymorphs of 2D-MoS_2 using alkali metal intercalation,[13−16] electron-beam irradiation,[17] straining,[18] high-pressure flux,[19,20] and electron doping.[21−24] Most of the known phase-transition methods for MoS_2 are limited to a single layer,[13−21] and among them, only the alkali-metal intercalation method could induce complete phase transition from 2H to 1T′ MoS_2.[13−16] However, the resulting 1T′ phase due to alkali-metal intercalation method can undergo oxidation and experiences impurity-induced strain in the host lattice; in addition, the phase transition was spatially incomplete, mostly due to a random intercalation of alkali atoms. The other processes mentioned above result in coexisting metallic and semiconductor phases, even for single-layer MoS_2.[17−21] Therefore, an efficient and direct way for the phase engineering of bulk 2H MoS_2 is necessary.

Recently, bulk 2H $MoTe_2$ has been converted into the 1T′ phase just by making the heterostructures with a 2D electride material, dicalcium nitride $[Ca_2N]^+\cdot e^-$, to realize the solid-state doping of 2D-TMDs with deeply penetrating high-density electrons.[24] Because $[Ca_2N]^+\cdot e^-$ is a layered material with a very low work function of 2.6 eV and contains layers of freely mobile electrons sandwiched between $[Ca_2N]^+$ layers at room temperature, it can transfer a high concentration of electrons ($\sim 10^{14}$ cm^{-2}) to the material it is in contact with.[24−26] Here

Received: October 11, 2019
Accepted: November 22, 2019
Published: November 22, 2019

DOI: 10.1021/acsnano.9b08037
ACS Nano 2019, 13, 14437−14446

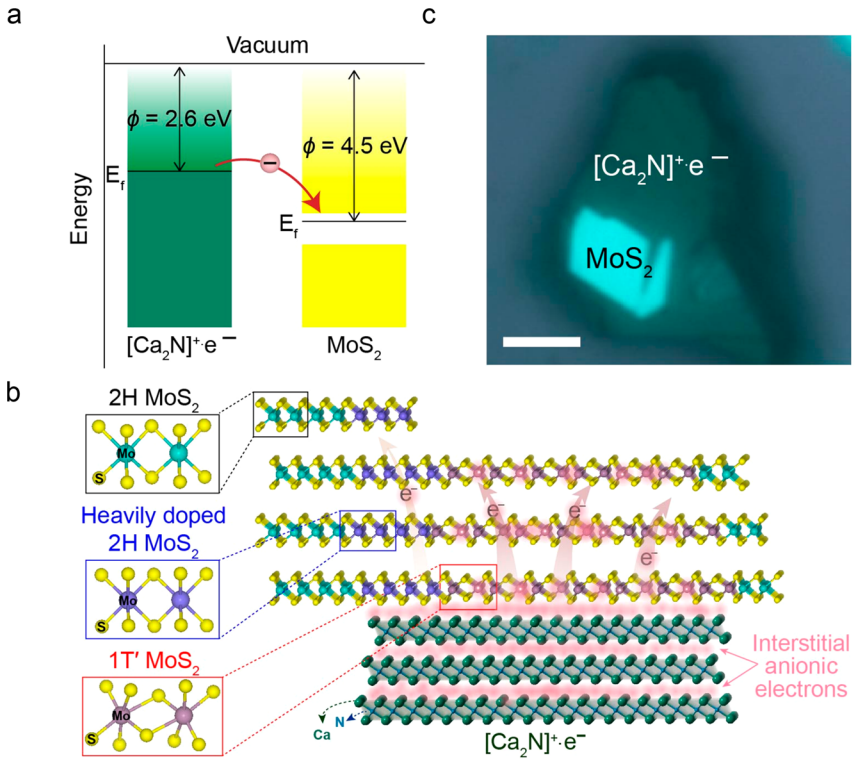

Figure 1. Charge injection from 2D-$[Ca_2N]^+\cdot e^-$ to bulk MoS_2 to induce phase transition. (a) Band alignment between $[Ca_2N]^+\cdot e^-$ and MoS_2 with work functions of 2.6 and 4.5 eV. (b) A schematic describing that electron injection from $[Ca_2N]^+\cdot e^-$ induces a 2H to 1T′ phase change in bulk MoS_2; MoS_2 is heavily doped in the thicker sections. (c) Optical view of a typical heterostructure of MoS_2 on 2D-$[Ca_2N]^+\cdot e^-$. The scale bar is 5 μm.

we note that the difference in work function between $[Ca_2N]^+\cdot e^-$ and MoS_2 is higher (>2 eV) than that between $[Ca_2N]^+\cdot e^-$ and $MoTe_2$ (1.3 eV),[24,27] which suggests that the kinetic energy of the doped surface electrons is larger in MoS_2; furthermore, a high density of electrons can be injected into bulk MoS_2 by heterostructuring with $[Ca_2N]^+\cdot e^-$. While previous surface electron-doping methods such as chemical functionalization or electrical gating were applied mostly for monolayer TMDs, they resulted in only a moderate (30 to 50 meV) bandgap reduction,[2−7,28,29] and complete metallization of bulk MoS_2 could not be achieved.

In this study, we report a series of lattice symmetry changes from the hexagonal phase to a distorted octahedral phase in bulk MoS_2 induced by the injection of a very high density of electrons by making the solid-state heterostructures with 2D-$[Ca_2N]^+\cdot e^-$ crystals. The resultant degenerate electron doping, at an estimated sheet density of $\sim 10^{14}$ cm^{-2}, penetrates tens of nanometers into bulk MoS_2 from the contact interface, leading to the gradual evolution of lattice symmetry and band-structure renormalization in bulk MoS_2. These changes were analyzed by PL spectroscopy, Raman spectroscopy, and density functional theory (DFT) calculations. We could observe several distinct phases of MoS_2, including heavily doped 2H, metallic phase (1T′), and possibly a combination of both hexagonal and 1T′-phases, which exhibited strong PL emission due to weak interlayer interactions. Our results illustrate the exceptionally controlled lattice symmetry and electronic band structure of MoS_2 forming the heterostructures with 2D-$[Ca_2N]^+\cdot e^-$.

RESULTS AND DISCUSSION

The schematic in Figure 1a indicates a large work function difference (~2 eV) between $[Ca_2N]^+\cdot e^-$ and MoS_2 owing to the electrons in $[Ca_2N]^+\cdot e^-$ can be easily injected into MoS_2 across the contact area with a high kinetic energy. These electrons penetrate deep into the bulk structure,[24] resulting in a structural change in MoS_2 from 2H to a metallic state with a distorted lattice (1T′) as shown in the schematic Figure 1b. Figure 1c shows optical views of the typical heterostructures made by preparing MoS_2 crystals on $[Ca_2N]^+\cdot e^-$. We prepared such heterostructures in the argon atmosphere to prevent the oxidation of $[Ca_2N]^+\cdot e^-$ that can occur at the ambient environment. If $[Ca_2N]^+\cdot e^-$ is oxidized, the Raman spectrum is greatly modified and its electron-doping capability is compromised (see Supporting Information, Figure S1 for the Raman spectra of $[Ca_2N]^+\cdot e^-$ before and after oxidation). For confocal Raman and PL spectroscopy, we air-sealed the heterostructures by capping them with transparent cover glass in an argon atmosphere.

We first show the correlated Raman and PL spectra of pristine bulk MoS_2 and $MoS_2/[Ca_2N]^+\cdot e^-$ heterostructures. The representative optical images are shown in Figure 2a, and the corresponding Raman and PL spectra obtained from these regions are displayed in Figure 2b,c, respectively. The Raman spectrum of pristine MoS_2 (Figure 2b, black curve) includes characteristic E_{2g}^1 and A_{1g} phonon modes at 382 and 408 cm^{-1} respectively, confirming the bulk thickness 2H MoS_2 crystals[1−5] (see Supporting Information, Figure S2 for thickness verification). Based on the complete absence of a $[Ca_2N]^+\cdot e^-$ Raman peak, it is deduced that the thickness of MoS_2 in Figure 2 is greater than ~30 nm (equal to the laser-penetration depth of MoS_2 at 514.5 nm).[30] The Raman spectra of bulk MoS_2 on $[Ca_2N]^+\cdot e^-$ exhibited softening in the A_{1g} and E_{2g}^1 modes to different extents (Figure 2b). Maximum red-shift values of 10 and 8 cm^{-1} were observed for the A_{1g} and E_{2g}^1

DOI: 10.1021/acsnano.9b08037
ACS Nano 2019, 13, 14437−14446

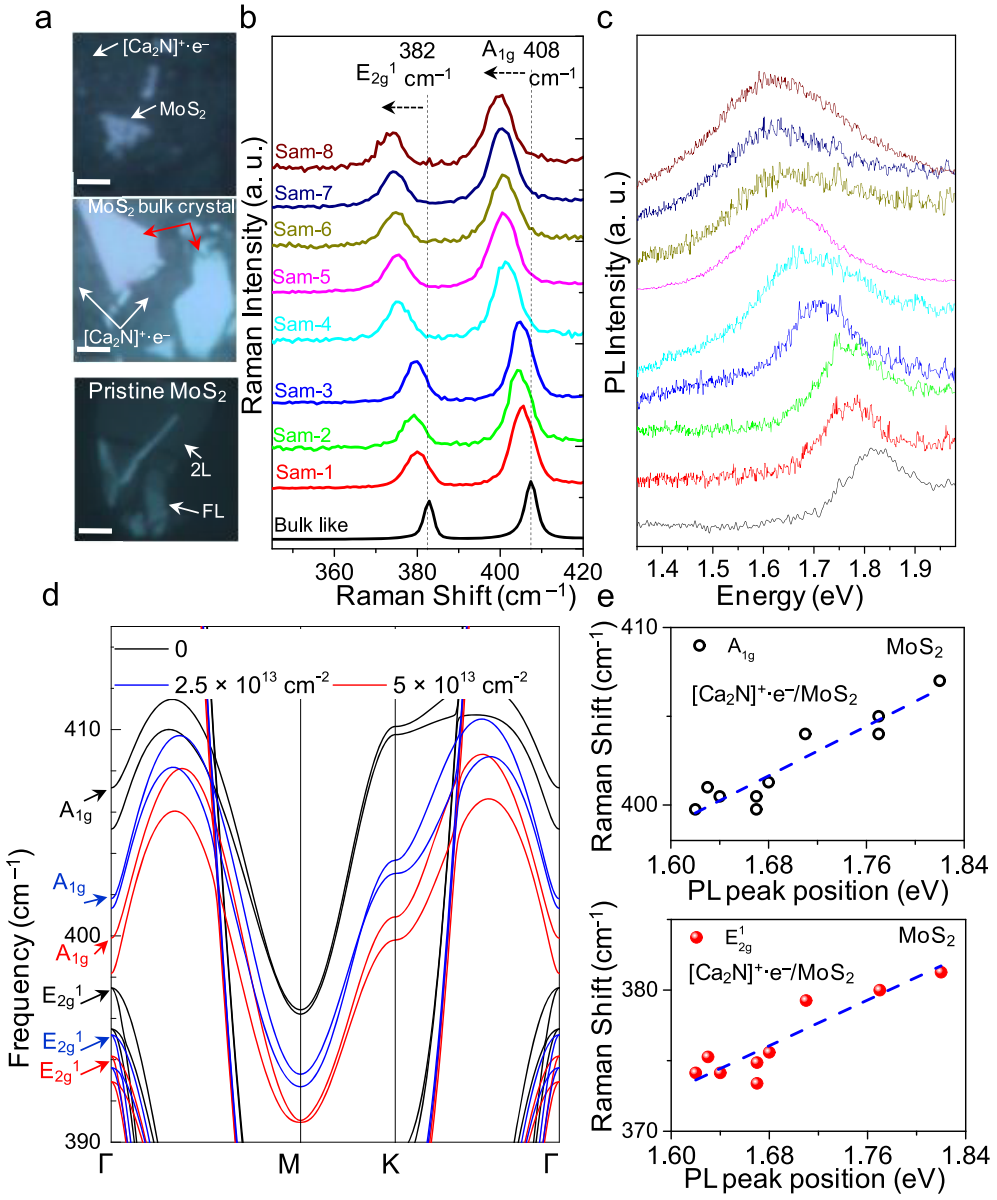

Figure 2. Renormalization of the optical bandgap and phonon energies of MoS_2 by electron injection. (a) Optical views of the MoS_2/$[Ca_2N]^+\cdot e^-$ heterostructure (scale bar = 5 μm). (b) Raman and (c) PL spectra obtained from eight different MoS_2/$[Ca_2N]^+\cdot e^-$ heterostructures. The dotted line act as a visual guide. Color-coded Raman and PL spectra were obtained from the same locations. (d) Phonon dispersion curves of undoped and doped (electron density (n) = 2.5 × 10^{13} and 5 × 10^{13} cm^{-2}) 2L-MoS_2. A_{1g} and $E_{2g}{}^1$ Raman frequencies are indicated by the arrow. (e) Correlation plots between $E_{2g}{}^1$ and A_{1g} phonon frequencies and the exciton peaks obtained from eight samples.

phonon modes, respectively. The red-shift of A_{1g} peak in the heterostructure as compared to the pristine value (408 cm^{-1} for bulk) could be attributed to electron transfer from 2D-$[Ca_2N]^+\cdot e^-$ to MoS_2. According to previous studies, observed softening in the A_{1g} mode (10 cm^{-1}) corresponds to an electron density of ~5 × 10^{13} cm^{-2},[2−7] demonstrating that direct injection of degenerate electrons in MoS_2 was achieved using 2D-$[Ca_2N]^+\cdot e^-$. We believe that the A_{1g} frequency shift (ranging 0−10 cm^{-1}) originates from the varying local thickness of MoS_2 on $[Ca_2N]^+\cdot e^-$. The thinner the MoS_2 flake is, the greater is the expected doping effect. This is because a finite amount of doping electrons are injected from 2D-$[Ca_2N]^+\cdot e^-$; such dependence of doping electron density on semiconductor thickness was previously observed with MoS_2[7] and $MoTe_2$.[24]

We also noticed a significant red-shift in the $E_{2g}{}^1$ mode of MoS_2 placed on $(Ca_2N)^+\cdot e^-$. Generally the change of the $E_{2g}{}^1$ mode energy was interpreted as the presence of a strain.[30,31] It is to be noted that that the in-plane lattice mismatch between 2D-$[Ca_2N]^+\cdot e^-$ and MoS_2 cannot cause such a large strain, because previously lattice mismatch with various substrates or hetero van der Waals layers were reported to cause less than 2 cm^{-1} of peak shift of $E_{2g}{}^1$ mode in thin (1−2 nm) MoS_2.[31−35] Therefore, the large softening amounting to ~8 cm^{-1} for the $E_{2g}{}^1$ mode indicates a significant strain and structural changes due to electron doping by 2D-$[Ca_2N]^+\cdot e^-$. Previously, doping with degenerate electrons was predicted to cause structural

DOI: 10.1021/acsnano.9b08037
ACS Nano 2019, 13, 14437−14446

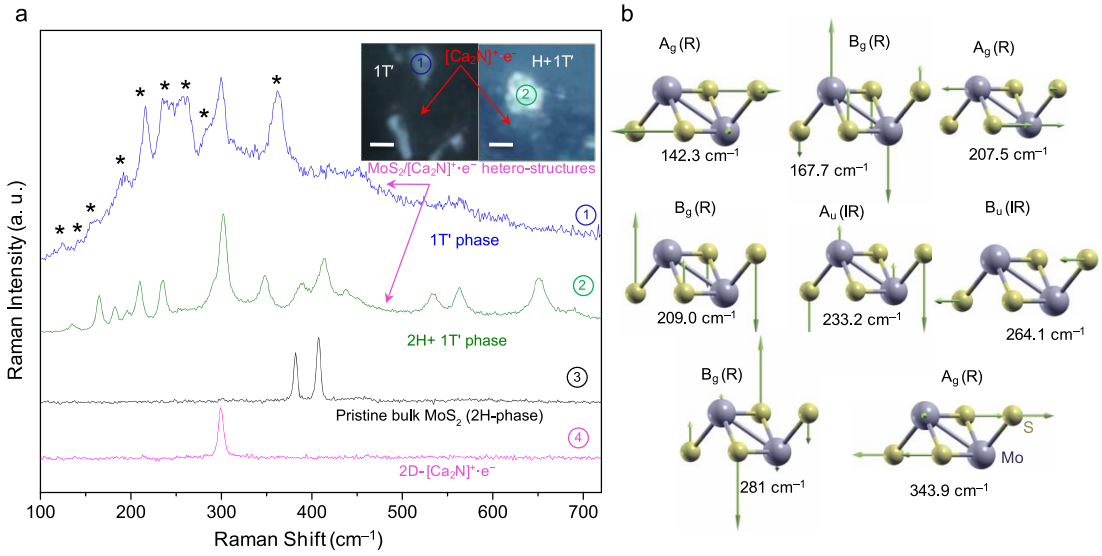

Figure 3. MoS_2 phase transition from 2H to 1T′. (a) Raman spectra of two different $MoS_2/[Ca_2N]^+\cdot e^-$ heterostructures (spectra 1 and 2), pristine bulk MoS_2 (black curve, spectrum 3), and $[Ca_2N]^+\cdot e^-$ (spectrum 4). Optical views of $MoS_2/[Ca_2N]^+\cdot e^-$ heterostructures representing spectra 1 and 2 are shown in the inset (scale bar = 5 μm). (b) Assignment of the Raman vibrational modes of 1T′ MoS_2 obtained from theoretical calculations.

changes and plasma screening of coulomb interactions, thus causing phonon softening in 1L-MoS_2.[22,36,37] In Figure 2d, we show the phonon dispersion relationship of bilayer MoS_2 calculated by DFT at an electron density of 5×10^{13} cm^{-2}; it predicts red-shifts of 7 and 4 cm^{-1} for the Raman A_{1g} and $E_{2g}{}^1$ modes, respectively, thus affirming that the observed giant softening of Raman modes may be attributed to the high density of electrons injected from $2D\text{-}[Ca_2N]^+\cdot e^-$ (see the calculated phonon dispersion curves at other electron densities in Supporting Information, Figures S3 and S4).

Interestingly, we observed a direct correlation between the red-shift of Raman peaks and PL peak positions. In Figure 2c, we display PL spectra obtained simultaneously with Raman spectra (Raman and PL spectra obtained from the same sample locations are color-coded). We found that the sample with a large red-shift for the Raman peak displayed a large PL peak shift. Correlated optical bandgap *vs* $E_{2g}{}^1$ or A_{1g} Raman frequency plots displayed a linear correlation as shown in Figure 2e. An optical bandgap reduction of ∼200 meV was observed for the sample with the maximum phonon softening of ∼10 and ∼8 cm^{-1} for the A_{1g} and $E_{2g}{}^1$ modes, respectively, indicating that electron injection by heterostructuring with $2D[Ca_2N]^+\cdot e^-$ caused giant renormalization in the bandgap and phonon modes of bulk MoS_2.

In Figure 3a, we show the Raman spectra of relatively thinner MoS_2 flakes on $[Ca_2N]^+\cdot e^-$ (spectra 1 and 2), which are vastly different from that of 2H phase MoS_2 (spectrum 3). We believe that the layer thickness of MoS_2 shown in Figure 3a is <30 nm (penetration depth of the excitation laser) and the thickness of the samples shown in Figure 2, because a peak at ∼300 cm^{-1} corresponding to $[Ca_2N]^+\cdot e^-$ could still be observed, unlike in the case of the Raman spectra in Figure 2b (see the non-normalized Raman spectra of $MoS_2/[Ca_2N]^+\cdot e^-$ heterostructures and bare $[Ca_2N]^+\cdot e^-$ in Supporting Information, Figure S5). The Raman spectrum of bare $[Ca_2N]^+\cdot e^-$ is shown for reference (spectrum 4). We should emphasize here that spectra 1 and 2 were obtained still from the bulk thickness of MoS_2; the optical contrast of the topmost MoS_2 layer in the heterostructure (shown in the inset of Figure 3a) is greater than that of pristine bulk MoS_2 (see the Raman spectra of pristine bulk MoS_2 in Supporting Information, Figure S5; its optical contrast was compared to that of the sample in Figure 3a). In thinner bulk MoS_2, we expect that the electron doping density is higher than 5×10^{13} cm^{-2}, which is the value estimated for the samples shown in Figure 2 and may have reached ∼10^{14} cm^{-2}, a value high enough to cause transition to 1T′ MoS_2.[4,13−15,21] First, we noticed in spectra 1 and 2 that the $E_{2g}{}^1$ and A_{1g} Raman modes, which are characteristic of 2H MoS_2, disappeared completely and instead, multiple Raman peaks newly emerged. In spectrum 2, we identified 17 Raman modes as corresponding to the 1T′ phase (B_g: 167 (J_1) and 236 (J_2) cm^{-1} and A_g: 138, 212, and 350 (J_3) cm^{-1} modes) Raman modes, infrared (IR) active phonon modes at 290 (E_u + E_{1g}), 393 (E_{1u}), and 420 cm^{-1} ($B_{2g}{}^2$ + $E_{1u}{}^2$), and 2H Raman modes ($B^2{}_{2g}$: 415 cm^{-1}, $E_{2g}{}^2$: 440 cm^{-1}, 2LA (M): 454 cm^{-1}, E_g (M) + TA (M): 535 cm^{-1}, E_{1g}: 564 cm^{-1}, A_g (M) + LA (M): 653 cm^{-1}, and B_{3g}: 693 cm^{-1}), thus suggesting a metaphase different from 2H or 1T′ MoS_2 crystals.[17−22,36−48] Details of Raman-peak assignment are provided in Table S1. Indeed, the observation of a large number of Raman peaks even with off-resonance laser excitation (2.41 eV) indicates that this particular thickness of MoS_2 on $[Ca_2N]^+\cdot e^-$ possesses low crystal symmetry, similar to other 2D semiconductors such as rhenium disulfide and rhenium diselenide, which normally exist in the 1T′ phase.[49,50] Another possible reason for the emergence of multiple Raman modes is the formation of a twisted multilayer MoS_2 structure due to a heavy electron doping density, which weakens interlayer attractions (will be discussed later). Because supercell structures are formed in twisted multilayer MoS_2, the zone-folding effect generates multivibration modes at the γ point, activating multiple Raman modes, as observed in twisted bilayer MoS_2 or graphene.[40,51]

In spectrum 1, the Raman modes of the metallic phase (1T′) were dominant, while the Raman modes of the 2H phase could not be observed; this is similar to the spectrum of 1T′ MoS_2

DOI: 10.1021/acsnano.9b08037
ACS Nano 2019, 13, 14437−14446

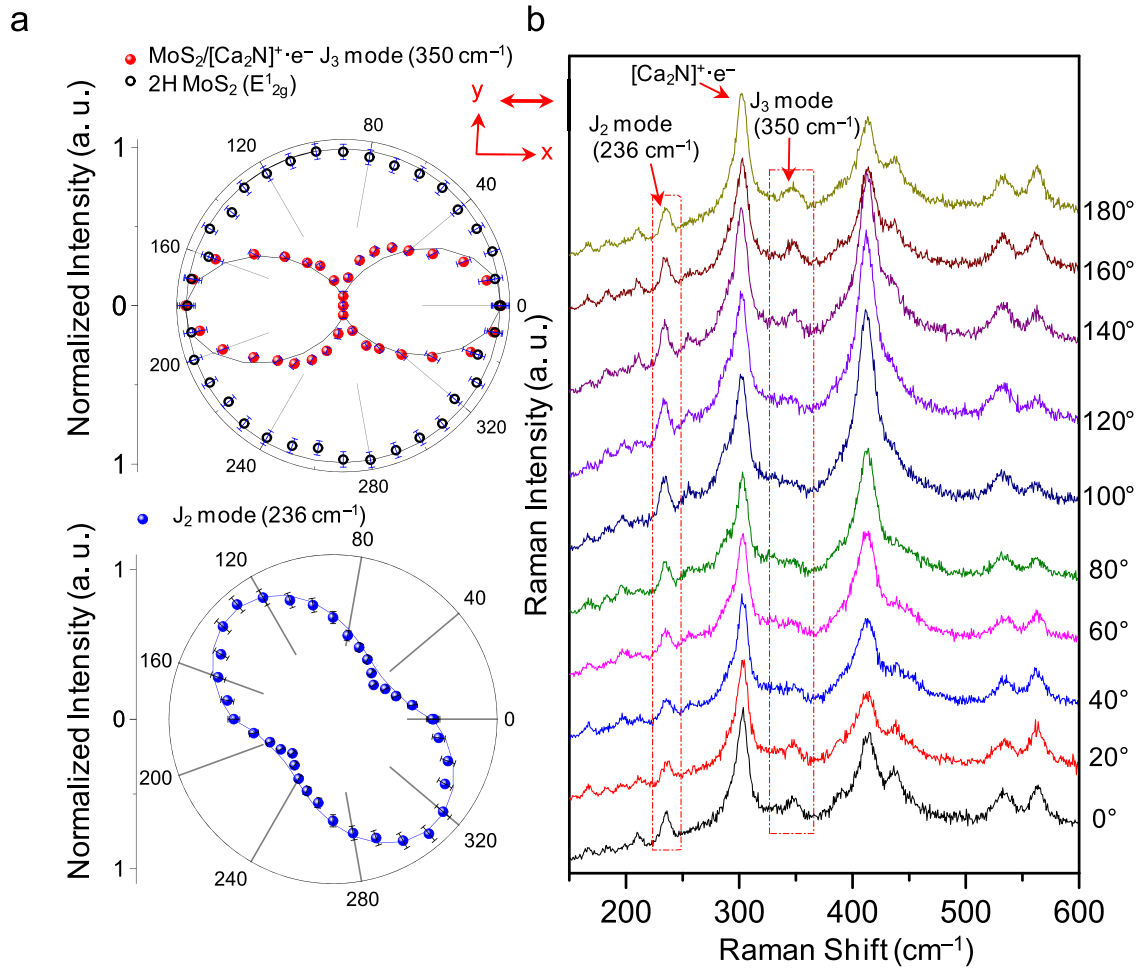

Figure 4. Anisotropic Raman response of the distorted lattice of bulk MoS_2 due to electron doping from $[Ca_2N]^+ \cdot e^-$. (a) Polar plots of the polarization-dependent Raman intensities of 2H MoS_2 (E_{2g}^1 mode), J_3 mode at 350 cm^{-1}, and J_2 mode at 236 cm^{-1} of bulk MoS_2 on $[Ca_2N]^+ \cdot e^-$ (see the main text for the measurement scheme). An angle of 0° represents a horizontal placement of the sample stage. The polar plot of the E_{2g}^1 mode is shown for comparison. Solid lines are fitted calculations using the Raman tensors of E_{2g}^1 mode of 2H MoS_2 and A_g mode of 1T′ MoS_2 and the experimental polarization configuration (see the main text). (b) Raman spectra at several selected rotation angles are shown.

obtained by Li-intercalation,[13] indicating that MoS_2 on $[Ca_2N]^+ \cdot e^-$ was converted completely into the 1T′ phase. The phonon modes of 1T′ MoS_2 were theoretically calculated. Considering the doped condition of MoS_2, we assumed an electron density of 2.2×10^{14} cm^{-2} for calculating the vibration modes of 1T′-MoS_2. We found that the observed Raman spectrum of 1T′-MoS_2 (spectrum 1 in Figure 3a) matched well with our calculated 1T′ MoS_2 in terms of the position and number of Raman modes, signifying that a very high level of electron injection (~10^{14} cm^{-2}) at the $MoS_2/[Ca_2N]^+ \cdot e^-$ heterostructure to yield a 1T′ MoS_2 lattice structure. Several 1T′ MoS_2 modes, identified in our calculation, are indicated by (*) in Figure 3a, and their vibration modes are displayed in Figure 3b (refer to Supporting Information, Table S2 for the assignment of all other Raman modes corresponding to 1T′ MoS_2).

Even thinner MoS_2, of which thickness we believe is only a few nanometers based on the nonattenuation of Raman peak at ~300 cm^{-1} of underneath $[Ca_2N]^+ \cdot e^-$ and the appeared optical contrast, displayed only two Raman peaks of A_g mode of 1T′ lattice at 146 cm^{-1} and the IR-active mode at 255 cm^{-1} with all other 1T′ specific Raman modes totally quenched (See the Supporting Information, Figure S6). Such distinct quenching of 1T′ lattice Raman modes with strong electron doping was not observed in electrolyte-doped[4,52] or Li-intercalated TMDs[13] and suggests that this particular MoS_2 on $[Ca_2N]^+ \cdot e^-$ may have reached a highly conducting phase or a lattice disordered phase due to excessive electron density.[53]

Though the exact origin of Raman spectra containing both 1T′ and 2H specific modes (spectrum 2 in Figure 3a) is not clearly known, we found that these modes are highly polarization-dependent. We obtained a series of Raman spectra while rotating the sample between a fixed polarizer and analyzer in the same direction as the horizontal *x*-axis of the sample stage of our Raman microscope. The polar plots of the Raman intensity of J_3 and J_2 modes are shown in Figure 4a, and Raman spectra at several selected rotation angles are displayed in Figure 4b, in which the angles represent sample rotation angles from the horizontal *x*-axis of the sample stage. The polarization dependence of the E_{2g}^1 mode of pristine bulk 2H MoS_2 is displayed for comparison in Figure 4a; it exhibited an isotropic response under the polarization-resolved Raman measurement as shown in Figure 4a (black circles). Raman spectra at all the measured angles for pristine 2H MoS_2 are included in Supporting Information, Figure S7. The isotropic response of the E_{2g}^1 mode of pristine 2H MoS_2 is expected

DOI: 10.1021/acsnano.9b08037
ACS Nano 2019, 13, 14437−14446

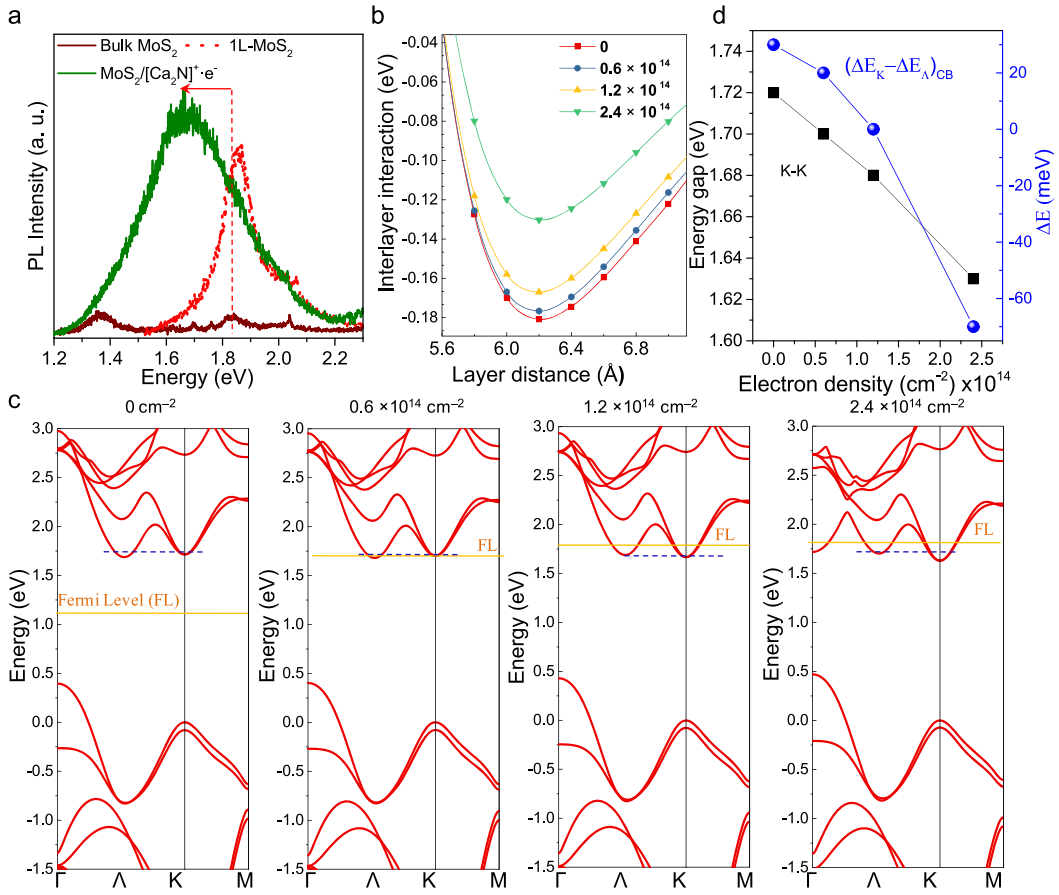

Figure 5. MoS_2 band-structure modulation due to the degenerate electron doping by $[Ca_2N]^+ \cdot e^-$. (a) PL spectra of pristine 1L-MoS_2 (red line), pristine bulk MoS_2 (brown line), and $MoS_2/[Ca_2N]^+ \cdot e^-$. The $MoS_2/[Ca_2N]^+ \cdot e^-$ structure displayed a broad red-shifted (by ~200 meV) PL intensity greater than that of pristine 1L-MoS_2. (b) Interlayer coupling energies calculated for 2L-MoS_2 at three different doping densities. Interlayer interaction of 2L-MoS_2 decreases with increasing doping density. (c) Electronic band structures of 2L-MoS_2 calculated at various doping densities. Note the gradual lowering (raising) of the CBV at the K (Λ) point with an increase in electron density. (d) Plot of the doping density-dependent bandgap reduction at the K point (black squares) and energy difference in the CBV at the K and Λ points ($\Delta E_k - \Delta E_\Lambda$) (blue balls).

because of its isotropic lattice structure.[47,48] On the contrary, the J_3 mode at 350 cm^{-1} and J_2 mode at 236 cm^{-1} in the Raman spectrum of thinner bulk MoS_2 on $[Ca_2N]^+ \cdot e^-$ were highly dependent on sample rotation under the polarized Raman measurement as shown in Figure 4a,b. Polarization dependence of A_g modes of 1T′ $MoTe_2$ is given by[23,54,55]

$$I = [c + (b - c)\cos^2\theta]^2$$

where I represents the Raman intensity, b and c the diagonal elements of the A_g mode Raman tensor, and θ represents the angle between the crystalline axis and the parallel polarization directions of the incident and the scattered light. Previously, bifold anisotropy of polarized Raman scattering was observed in distorted octahedral lattices such as ReS_2 and $ReSe_2$,[49,50] and the anisotropy factor (b/c) of 2.3 was obtained for 1T′ $MoTe_2$.[23] Our DFT calculation suggests that the A_g mode of 1T′ MoS_2 must have the similar dependence, but the anisotropy factor has not been estimated so far. We fitted the observed poarization dependence of J_3 mode and J_2 modes with the above equation, and the anisotropy factors were estimated to be 2.4 and 1.9, respectively, which confirms that this specific bulk MoS_2 underwent phase transition from a 2H hexagonal lattice to a distorted octahedral lattice upon electron injection by 2D-$[Ca_2N]^+ \cdot e^-$.

$MoS_2/[Ca_2N]^+ \cdot e^-$ that displayed the spectrum 1 in Figure 3a was characterized to be a completely metallic phase and it exhibited no detectable PL intensity, which is consistent with the zero gap metallic structure of 1T′ MoS_2.[13,21,22] In contrast, we observed unusually strong PL from bulk MoS_2 that displayed both 2H and 1T′ specific Raman modes (spectrum 2 in Figure 3a); the observed PL intensity is even greater than the PL intensity of pristine monolayer MoS_2, whereas the PL intensity of the pristine bulk MoS_2 is much smaller than that of monolayer MoS_2 as shown in Figure 5a and Supporting Information, Figure S2. We performed the differential reflectance mapping on these samples (see the Supporting Information, Figure S8) and found that absorption and the surface quality were similar to pristine bulk MoS_2, which excludes the roles of higher absorption or scattering to observed strong PL from $MoS_2/[Ca_2N]^+ \cdot e^-$. The PL peak position of this MoS_2 was located at 1.63 eV, ~200 meV lower than the original peak position corresponding to the direct transition of bulk MoS_2 at the K-point of the Brillouin zone. The brown line in the Figure 5a, shows the PL spectrum of pristine bulk MoS_2 with distinct PL emission at 1.82 and 1.35

DOI: 10.1021/acsnano.9b08037
ACS Nano 2019, 13, 14437−14446

eV, which could be attributed to the transitions along the K−K and Λ−Γ lines, respectively.[1,56] Our observations suggest that long-range electron injection may have resulted in a meta-phase MoS_2 with weak interlayer coupling and strong PL.

To describe the origin of various footprints of lattice evolution due to long-range electron injection, we performed DFT calculations on the electronic band structure of bilayer MoS_2 with increasing electron doping density to simulate electron transfer from $[Ca_2N]^+\cdot e^-$, and the results are shown in Figure 5b–d. First, in Figure 5b, we show the variation in the interlayer coupling of bilayer MoS_2 with respect to electron density. Interlayer coupling reached its minimum value at ∼0.62 nm, which is the typical interlayer distance of 2L-MoS_2 at 0 doping density. While this interlayer distance was insensitive to doping concentration, interlayer coupling at this distance gradually decreased from −0.18 to −0.13 eV as the doped electron density increased from 0 to 2.4×10^{14} cm^{-2}, suggesting interlayer decoupling in MoS_2. Such decoupling has a direct effect on the electronic band structure. In Figure 5c, we show the band structures of 2L-MoS_2 calculated at electron densities of 0, 0.6×10^{14}, 1.2×10^{14}, and 2.4×10^{14} cm^{-2}. It is to be noted that the valence band at the K point was taken as the reference for all calculations. We noticed that the conduction band valley (CBV) at the K-point lowered monotonically with an increase in electron density, exhibiting a 90 meV bandgap reduction at the K-point at an electron density of 2.4×10^{14} cm^{-2}. A plot of K−K transition energy *vs* electron density is shown in Figure 5d. The observed reduction in K−K transition energy with an increase in electron density is consistent with the observation of large red-shift of the PL peak of $MoS_2/[Ca_2N]^+\cdot e^-$ heterostructures. In contrast, our calculations showed that the CBV at the Λ point increased with an increase in electron density (indicated by a horizontal dashed line in Figure 5c). As a result, at an electron density of 1.2×10^{14} cm^{-2}, direct bandgap energy at the K−K point is equal to the indirect band (Λ−Γ) gap energy. At 2.4×10^{14} cm^{-2}, the difference ($\Delta E_k - \Delta E_\Lambda$) between Λ-K and K−K energy gaps was −70 meV, as shown in Figure 5d. Our DFT results on the inversion between Λ-K and K−K energy gaps with respect to an increase in the electron density are consistent with previously calculated band structures of MoS_2 at high electron concentrations.[36,52] Meanwhile, the minimum energy of the conduction band shifted from the Λ point to the K point due to electron doping, which enhances the PL signal at the K-valley as suggested by the previously reported local strain-induced band gap modulation in bulk TMD crystal,[56] although the indirect band gap in TMDs (Γ−K) was maintained, similar to the doping concentration-dependent band structure of 2L-MoS_2 (Figure 5c). Another possible explanation for the strong PL of bulk MoS_2 at high electron densities could be the formation of twisted bulk MoS_2 due to weaker interlayer coupling, as suggested by the multiple phonon modes observed in Raman measurements (Figure 3a).[57] The band structure of twisted bulk MoS_2 may be different from that calculated for the AB stacking bilayer in Figure 5c; the position of the topmost valence band at the Γ point in the twisted structure is supposed to be down-shifted to a greater extent than that in the case of AB stacking.[58] We conjecture that the twisted band structure may be responsible for the stronger PL signal of bulk MoS_2 at the K-point than that observed with AB stacking. Our calculations provide a convincing explanation for the structural modulation of bulk MoS_2 by injecting electrons from $[Ca_2N]^+\cdot e^-$, implying that strong doping can lead to a giant bandgap renormalization. The greatly enhanced PL emission of bulk MoS_2 may be attributed to the formation of twisted multilayer MoS_2 due to the decoupling of interlayer interactions.

CONCLUSIONS

In summary, we demonstrated the complete phase conversion of bulk MoS_2 from 2H to 1T′ by preparing heterostructures with 2D-$[Ca_2N]^+\cdot e^-$. This conversion was confirmed by the presence of metallic-phase Raman modes and their polarization dependency. We observed a giant band structure renormalization (>200 meV) due to degenerate electron doping by charge injection from 2D-$[Ca_2N]^+\cdot e^-$. We also observed a large softening of Raman modes and strong PL intensity in the vicinity of the metallic regime, suggesting weakened interlayer coupling in electron-injected bulk MoS_2, which was further confirmed by DFT calculations. Our demonstration of giant bandgap renormalization, complete metallization, and facile phase engineering of bulk MoS_2 using 2D$[Ca_2N]^+\cdot e^-$ as the substrate provides clear snapshots of the intriguing phase-transition process of MoS_2 due to direct electron injection from solid-state 2D electrides and helps to develop 2D materials of diverse phases of electrical and optical properties.

EXPERIMENTAL METHODS

Synthesis of Dicalcium Nitride $[Ca_2N]^+\cdot e^-$. Two-dimensional crystals of $[Ca_2N]^+\cdot e^-$ were synthesized using a previous protocol on the solid-state reaction between calcium nitride (Ca_3N_2) powders and calcium metal.[25,26] A mixture of Ca_3N_2 powders and calcium chips at a molar ratio of 1:1 was pressed into a pellet at a pressure of 20–30 MPa. The pellet was fully covered with molybdenum foil and annealed at 800 °C for 48 h under vacuum (∼10^{-3} Pa), after which the sample was quenched with water. The obtained $[Ca_2N]^+\cdot e^-$ was ground into powder in an agate mortar in a nitrogen-filled glovebox and reannealed at 800 °C for 48 h under vacuum to improve homogeneity.

Preparation of the Heterostructure Using $[Ca_2N]^+\cdot e^-$ and 2H MoS_2. We first exfoliated bulk $[Ca_2N]^+\cdot e^-$ crystals using the scotch-tape method onto a glass slide as the substrate in an argon environment and then heated them at 80 °C. Later, we conducted the exfoliation of bulk 2H MoS_2 (2D Semiconductor Supplies Corp.) on a polydimethylsiloxane (PDMS) substrate. Exfoliated MoS_2 on the PDMS substrate was directly transferred onto pre-exfoliated 2D-$[Ca_2N]^+\cdot e^-$ to obtain the desired heterostructure. The sample was heated at 80 °C to ensure strong contact between MoS_2 crystals and $[Ca_2N]^+\cdot e^-$. The entire sample-preparation process was carried out in an argon gas environment to prevent the oxidation of $[Ca_2N]^+\cdot e^-$. Finally, the heterostructure samples were air-sealed for in-air optical characterization by capping with a cover glass.

PL and Raman Spectral Measurements. Confocal PL and Raman spectral measurements were performed on a lab-made confocal microscope system.[7] An argon laser (514.5 nm) was used at a laser power of 500 μW for obtaining the Raman and PL spectra. An objective lens with a numerical aperture of 0.95 was used to illuminate the samples and collect the scattered light. The collected light was guided to a 50 cm-long monochromator equipped with a cooled charge-coupled device through an optical fiber with a core diameter of 100 μm; this acted as a confocal detection pinhole. Diffraction gratings with 150 and 1800 grooves mm^{-1} were used for PL and Raman measurements, respectively.

DFT Calculation Methods. The electronic band structure of bilayer MoS_2 was investigated by DFT analysis performed using Quantum Espesso code.[59] Ultrasoft potentials were used in all calculations with a cutoff energy of 60 Ry. A Monkhorst–Pack *k*-grid (24 × 24 × 1) was used to optimize the cell structure at a pressure and force <0.5 kbar and 10^{-3} Ry/Bohr, respectively. We implemented

DOI: 10.1021/acsnano.9b08037
ACS Nano 2019, 13, 14437−14446

the VDW-DF-OB86 functional to treat interlayer interactions between MoS_2 layers.[60−62]

ASSOCIATED CONTENT

Supporting Information

The Supporting Information is available free of charge at https://pubs.acs.org/doi/10.1021/acsnano.9b08037.

Raman spectra of dicalcium nitride crystals, PL and Raman spectra of MoS_2 films, theoretical evidence of degenerate electron doping induced phonon softening in the MoS_2 crystal, thickness estimation of the MoS_2 crystal placed on a $[Ca_2N]^+\cdot e^-$ substrate, assignment of Raman peak positions of $MoS_2/[Ca_2N]^+\cdot e^-$ heterostructures, Raman spectrum of the thin MoS_2 on the top of the $[Ca_2N]^+\cdot e^-$, polarization-dependent Raman vibrational modes of 2H MoS_2 and differential reflectance measurement (PDF)

AUTHOR INFORMATION

Corresponding Authors

*Email: ddloc@skku.edu.
*Email: kimsungwng@skku.edu.
*Email: j.kim@skku.edu.

ORCID

Kyungwha Chung: 0000-0002-6774-4720
Dinh Loc Duong: 0000-0002-4118-9589
Sung Wng Kim: 0000-0002-4802-5421
Jeongyong Kim: 0000-0003-4679-0370

Author Contributions

#These authors contributed equally to this work.

Notes

The authors declare no competing financial interest.

ACKNOWLEDGMENTS

J.K., S.W.K., and K.P.D. acknowledge the National Research Foundation of Korea (2019R1A2C1006586, 2015M3D1A1070639 and 2019R1I1A1A01063391) for the financial support. D.L.D. acknowledges the Institute for Basic Science (IBS-R011-D1) for the financial support.

REFERENCES

(1) Mak, K. F.; Lee, C.; Hone, J.; Shan, J.; Heinz, T. F. Atomically Thin MoS_2: A New Direct-Gap Semiconductor. *Phys. Rev. Lett.* **2010**, *105*, 136805.

(2) Wang, Q. H.; Kalantar-Zadeh, K.; Kis, A.; Coleman, J. N.; Strano, M. S. Electronics and Optoelectronics of Two-Dimensional Transition Metal Dichalcogenides. *Nat. Nanotechnol.* **2012**, *7*, 699−712.

(3) Mak, K. F.; He, K.; Lee, C.; Lee, G. H.; Hone, J.; Heinz, T. F.; Shan, J. Tightly Bound Trions in Monolayer MoS_2. *Nat. Mater.* **2013**, *12*, 207−211.

(4) Chakraborty, B.; Bera, A.; Muthu, D. V. S.; Bhowmick, S.; Waghmare, U. V.; Sood, A. K. Symmetry-Dependent Phonon Renormalization in Monolayer MoS_2 Transistor. *Phys. Rev. B: Condens. Matter Mater. Phys.* **2012**, *85*, 161403.

(5) Kiriya, D.; Tosun, M.; Zhao, P.; Kang, J. S.; Javey, A. Air-Stable Surface Charge Transfer Doping of MoS_2 by Benzyl Viologen. *J. Am. Chem. Soc.* **2014**, *136*, 7853−7856.

(6) Fang, H.; Tosun, M.; Seol, G.; Chang, T. C.; Takei, K.; Guo, J.; Javey, A. Degenerate *n*-Doping of Few-Layer Transition Metal Dichalcogenides by Potassium. *Nano Lett.* **2013**, *13*, 1991−1995.

(7) Dhakal, K. P.; Duong, D. L.; Lee, J.; Nam, H.; Kim, M.; Kan, M.; Lee, Y. H.; Kim, J. Confocal Absorption Spectral Imaging of MoS_2: Optical Transitions Depending on the Atomic Thickness of Intrinsic and Chemically Doped MoS_2. *Nanoscale* **2014**, *6*, 13028−13035.

(8) Ma, Y.; Kou, L.; Li, X.; Dai, Y.; Smith, S. C.; Heine, T. Quantum Spin Hall Effect and Topological Phase Transition in Two-Dimensional Square Transition-Metal Dichalcogenides. *Phys. Rev. B: Condens. Matter Mater. Phys.* **2015**, *92*, No. 085427.

(9) Duerloo, K. A. N.; Li, Y.; Reed, E. J. Structural Phase Transitions in Two-Dimensional Mo- and W-Dichalcogenide Monolayers. *Nat. Commun.* **2014**, *5*, 4214.

(10) Kappera, R.; Voiry, D.; Yalcin, S. E.; Branch, B.; Gupta, G.; Mohite, A. D.; Chhowalla, M. Phase-Engineered Low-Resistance Contacts for Ultrathin MoS_2 Transistors. *Nat. Mater.* **2014**, *13*, 1128−1134.

(11) Qi, Y.; Naumov, P. G.; Ali, M. N.; Rajamathi, C. R.; Schnelle, W.; Barkalov, O.; Hanfland, M.; Wu, S. C.; Shekhar, C.; Sun, Y.; Su, V.; Schmidt, M.; Schwarz, U.; Pippel, E.; Werner, P.; Hillebrand, R.; Förster, T.; Kampert, E.; Parkin, S.; Cava, R. J.; et al. Superconductivity in Weyl Semimetal Candidate $MoTe_2$. *Nat. Commun.* **2016**, *7*, 11038.

(12) Qian, X.; Liu, J.; Fu, L.; Li, J. Quantum Spin Hall Effect in Two-Dimensional Transition Metal Dichalcogenides. *Science* **2014**, *346*, 1344−1347.

(13) Tan, S. J. R.; Abdelwahab, I.; Ding, Z.; Zhao, X.; Yang, T.; Loke, G. Z. J.; Lin, H.; Verzhbitskiy, I.; Poh, S. M.; Xu, H.; Nai, C. T.; Zhou, W.; Eda, G.; Jia, B.; Loh, K. P. Chemical Stabilization of 1T′ Phase Transition Metal Dichalcogenides with Giant Optical Kerr Nonlinearity. *J. Am. Chem. Soc.* **2017**, *139*, 2504−2511.

(14) Eda, G.; Fujita, T.; Yamaguchi, H.; Voiry, D.; Chen, M.; Chhowalla, M. Coherent Atomic and Electronic Heterostructures of Single-Layer MoS_2. *ACS Nano* **2012**, *6*, 7311−7317.

(15) Enyashin, A. N.; Seifert, H. G. Density-Functional Study of Li_xMoS_2 Intercalates ($0 \le x \le 1$). *Comput. Theor. Chem.* **2012**, *999*, 13−20.

(16) Gordon, R. A.; Yang, D.; Crozier, E. D.; Jiang, D. T.; Frindt, R. F. Structures of Exfoliated Single Layers of WS_2, MoS_2, and $MoSe_2$ in Aqueous Suspension. *Phys. Rev. B: Condens. Matter Mater. Phys.* **2002**, *65*, 125407.

(17) Lin, Y. C.; Dumcenco, D. O.; Huang, Y. S.; Suenaga, K. Atomic Mechanism of Phase Transition Between Metallic and Semiconducting MoS_2 Single-Layers. *Nat. Nanotechnol.* **2014**, *9*, 391−396.

(18) Song, S.; Keum, D. H.; Cho, S.; Perello, D.; Kim, Y.; Lee, Y. H. Room Temperature Semiconductor-Metal Transition of $MoTe_2$ Thin Films Engineered by Strain. *Nano Lett.* **2016**, *16*, 188−193.

(19) Chi, Z. H.; Zhao, X. M.; Zhang, H.; Goncharov, A. F.; Lobanov, S. S.; Kagayama, T.; Sakata, M.; Chen, X. J. Pressure-Induced Metallization of Molybdenum Disulfide. *Phys. Rev. Lett.* **2014**, *113*, No. 036802.

(20) Nayak, A. P.; Pandey, T.; Voiry, D.; Liu, J.; Moran, S. T.; Sharma, A.; Tan, C.; Chen, C. H.; Li, L. J.; Chhowalla, M.; Lin, J. F.; Singh, A. K.; Akinwande, D. Pressure-Dependent Optical and Vibrational Properties of Monolayer Molybdenum Disulfide. *Nano Lett.* **2015**, *15*, 346−353.

(21) Yin, X.; Wang, Q.; Cao, L.; Tang, C. S.; Luo, X.; Zheng, Y.; Wong, L. M.; Wang, S. J.; Quek, S. Y.; Zhang, W.; Rusydi, A.; Wee, A. T. S. Tunable Inverted Gap in Monolayer Quasi-Metallic MoS_2 Induced by Strong Charge-Lattice Coupling. *Nat. Commun.* **2017**, *8*, 486.

(22) Zhuang, H. L.; Johannes, M. D.; Singh, A. K.; Hennig, R. G. Doping-Controlled Phase Transitions in Single-Layer MoS_2. *Phys. Rev. B: Condens. Matter Mater. Phys.* **2017**, *96*, 165305.

(23) Wang, Y.; Xiao, J.; Zhu, H.; Li, Y.; Alsaid, Y.; Fong, K. Y.; Zhou, Y.; Wang, S.; Shi, W.; Wang, Y.; Zettl, A.; Reed, E. J.; Zhang, X. Structural Phase Transition in Monolayer $MoTe_2$ Driven by Electrostatic Doping. *Nature* **2017**, *550*, 487−491.

(24) Kim, S.; Song, S.; Park, J.; Yu, H. S.; Cho, S.; Kim, D.; Baik, J.; Choe, D. H.; Chang, K. J. Y.; Lee, H.; Kim, S. W.; Yang, H. Long-Range Lattice Engineering of $MoTe_2$ by a 2D Electride. *Nano Lett.* **2017**, *17*, 3363−3368.

DOI: 10.1021/acsnano.9b08037
ACS Nano 2019, 13, 14437−14446

(25) Lee, K.; Kim, S. W.; Toda, Y.; Matsuishi, S.; Hosono, H. Dicalcium Nitride as a Two-Dimensional Electride with an Anionic Electron Layer. *Nature* **2013**, *494*, 336−340.
(26) Faseela, K. P.; Kim, Y. J.; Kim, S. G.; Kim, S. W.; Baik, S. Dramatically Enhanced Stability of Silver Passivated Dicalcium Nitride Electride: Ag-Ca_2N. *Chem. Mater.* **2018**, *30*, 7803−7812.
(27) Farmanbar, M.; Brocks, G. Ohmic Contacts to 2D Semiconductors Through Van Der Waals Bonding. *Adv. Electron. Mater.* **2016**, *2*, 1500405.
(28) Steinhoff, A.; Rösner, M.; Jahnke, F.; Wehling, T. O.; Gies, C. Influence of Excited Carriers on the Optical and Electronic Properties of MoS_2. *Nano Lett.* **2014**, *14*, 3743−3748.
(29) Ghimire, G.; Dhakal, K. P.; Neupane, G. P.; Jo, S. G.; Kim, H.; Seo, C.; Lee, Y. H.; Joo, J.; Kim, J. Optically Active Charge Transfer in Hybrids of Alq_3 Nanoparticles and MoS_2 Monolayer. *Nanotechnology* **2017**, *28*, 185702.
(30) Brotons-Gisbert, M.; Segura, A.; Robles, R.; Canadell, E.; Ordejón, P.; Sánchez-Royo, J. F. Optical and Electronic Properties of 2H-MoS_2 Under Pressure: Revealing the Spin-Polarized Nature of Bulk Electronic Bands. *Phys. Rev. Mater.* **2018**, *2*, No. 054602.
(31) Lloyd, D.; Liu, X.; Christopher, J. W.; Cantley, L.; Wadehra, A.; Kim, B. L.; Goldberg, B. B.; Swan, A. K.; Bunch, J. S. Band Gap Engineering with Ultralarge Biaxial Strains in Suspended Monolayer MoS_2. *Nano Lett.* **2016**, *16*, 5836−5841.
(32) Oakes, L.; Carter, R.; Hanken, T.; Cohn, A. P.; Share, K.; Schmidt, B.; Pint, C. L. Interface Strain in Vertically Stacked Two Dimensional Heterostructured Carbon-MoS_2 Nanosheets Controls Electrochemical Reactivity. *Nat. Commun.* **2016**, *7*, 11796.
(33) Zhao, M.; Liu, M.; Dong, Y.; Zou, C.; Yang, K.; Yang, Y.; Zhang, L.; Huang, S. Epitaxial Growth of Two-Dimensional $SnSe_2$/MoS_2 Misfit Heterostructures. *J. Mater. Chem. C* **2016**, *4*, 10215−10222.
(34) Zhao, M.; Zhang, W.; Liu, M.; Zou, C.; Yang, K.; Yang, Y.; Dong, Y.; Zhang, L.; Huang, S. Interlayer Coupling in Anisotropic/Isotropic Van Der Waals Heterostructures of ReS_2 and MoS_2 Monolayers. *Nano Res.* **2016**, *9*, 3772−3780.
(35) Liu, X.; Balla, I.; Bergeron, H.; Campbell, G. P.; Bedzyk, M. J.; Hersam, M. C. Rotationally Commensurate Growth of MoS_2 on Epitaxial Graphene. *ACS Nano* **2016**, *10*, 1067−1075.
(36) Fisher, H. First-Principles Investigation of Electron-Phonon Interactions in Novel Superconductors, *Ph.D. Thesis*, Oxford University, Oxford, UK, 2014.
(37) Cheng, Y.; Nie, A.; Zhang, Q.; Gan, L.-Y.; Shahbazian-Yassar, R.; Schwingenschlogl, U. Origin of the Phase Transition in Lithiated Molybdenum Disulfide. *ACS Nano* **2014**, *8*, 11447−11453.
(38) Livneh, T.; Spanier, J. E. A Comprehensive Multiphonon Spectral Analysis in MoS_2. *2D Mater.* **2015**, *2*, No. 035003.
(39) Xia, M.; Li, B.; Yin, K.; Capellini, G.; Niu, G.; Gong, Y.; Zhou, W.; Ajayan, P. M.; Xie, Y. H. Spectroscopic Signatures of AA′ and AB Stacking of Chemical Vapor Deposited Bilayer MoS_2. *ACS Nano* **2015**, *9*, 12246−12254.
(40) Lin, M. L.; Tan, Q. H.; Wu, J. B.; Chen, X. S.; Wang, J. H.; Pan, Y. H.; Zhang, X.; Cong, X.; Zhang, J.; Ji, W.; Hu, P. A.; Liu, K. H.; Tan, P. H. Moiré Phonons in Twisted Bilayer MoS_2. *ACS Nano* **2018**, *12*, 8770−8780.
(41) Stacy, A. M.; Hodul, D. T. Raman Spectra of IVB and VIB Transition Metal Disulfides Using Laser Energies Near the Absorption Edges. *J. Phys. Chem. Solids* **1985**, *46*, 405−409.
(42) Frey, G. L.; Tenne, R.; Matthews, M. J.; Dresselhaus, M. S.; Dresselhaus, G. Raman and Resonance Raman Investigation of MoS_2 Nanoparticles. *Phys. Rev. B: Condens. Matter Mater. Phys.* **1999**, *60*, 2883−2892.
(43) Jiao, Y.; Mukhopadhyay, A.; Ma, Y.; Yang, L.; Hafez, A. M.; Zhu, H. Ion Transport Nanotube Assembled with Vertically Aligned Metallic MoS_2 for High Rate Lithium-ion Batteries. *Adv. Energy Mater.* **2018**, *8*, 1702779.
(44) Mignuzzi, S.; Pollard, A. J.; Bonini, N.; Brennan, B.; Gilmore, I. S.; Pimenta, M. A.; Richards, D.; Roy, D. Effect of Disorder on Raman Scattering of Single-Layer MoS_2. *Phys. Rev. B: Condens. Matter Mater. Phys.* **2015**, *91*, 195411.
(45) Wu, H.; Yang, R.; Song, B.; Han, Q.; Li, J.; Zhang, Y.; Fang, Y.; Tenne, R.; Wang, C. Biocompatible Inorganic Fullerene Like Molybdenum Disulfide Nanoparticles Produced by Pulsed Laser Ablationin Water. *ACS Nano* **2011**, *5*, 1276−1281.
(46) Calandra, M. Chemically Exfoliated Single-Layer MoS_2: Stability, Sattice Dynamics, and Catalytic Adsorption from First Principles. *Phys. Rev. B: Condens. Matter Mater. Phys.* **2013**, *88*, 245428.
(47) Zheng, W.; Zhu, Y.; Li, F.; Huang, F. Raman Spectroscopy Regulation in Van Der Waals crystals. *Photonics Res.* **2018**, *6*, 991−995.
(48) Zhang, X.; Qiao, X. F.; Shi, W.; Wu, J. B.; Jiang, D. S.; Tan, P. H. Phonon and Raman Scattering of Two-Dimensional Transition Metal Dichalcogenides From Monolayer, Multilayer to Bulk Material. *Chem. Soc. Rev.* **2015**, *44*, 2757−2785.
(49) Chenet, D. A.; Aslan, O. B.; Huang, P. Y.; Fan, C.; van der Zande, A. M.; Heinz, T. F.; Hone, J. C. In-Plane Anisotropy in Mono- and Few-Layer ReS_2 Probed by Raman Spectroscopy and Scanning Transmission Electron Microscopy. *Nano Lett.* **2015**, *15*, 5667−5672.
(50) Arora, A.; Noky, J.; Drüppel, M.; Jariwala, B.; Deilmann, T.; Schneider, R.; Schmidt, R.; Del Pozo-Zamudio, O.; Stiehm, T.; Bhattacharya, A.; Krüger, P.; de Vasconcellos, S. M.; Rohlfing, M.; Bratschitsch, R. Highly Anisotropic In-Plane Excitons in Atomically Thin and Bulk Like 1T′-$ReSe_2$. *Nano Lett.* **2017**, *17*, 3202−3207.
(51) Jorio, A.; Cançado, L. G. Raman Spectroscopy of Twisted Bilayer Graphene. *Solid State Commun.* **2013**, *175*, 3−12.
(52) Sohier, T.; Ponomarev, E.; Gibertini, M.; Berger, H.; Marzari, N.; Ubrig, N.; Morpurgo, A. F. Enhanced Electron-Phonon Interaction in Multivalley Materials. *Phys. Rev. X* **2019**, *9*, No. 031019.
(53) Ovchinnikov, D.; Gargiulo, F.; Allain, A.; Pasquier, D. J.; Dumcenco, D.; Ho, C. H.; Yazyev, O. V.; Kis, A. Disorder Engineering and Conductivity Dome in ReS_2 with Electrolyte Gating. *Nat. Commun.* **2016**, *7*, 12391.
(54) Beams, R.; Cançado, L. G.; Krylyuk, S.; Kalish, I.; Kalanyan, B.; Singh, A. K.; Choudhary, K.; Bruma, A.; Vora, P. M.; Tavazza, F.; Davydov, A. V.; Stranick, S. J. Characterization of Few-Layer 1T′ $MoTe_2$ by Polarization-Resolved Second Harmonic Generation and Raman Scattering. *ACS Nano* **2016**, *10*, 9626−9636.
(55) Ma, X.; Guo, P.; Yi, C.; Yu, Q.; Zhang, A.; Ji, J.; Tian, Y.; Jin, F.; Wang, Y.; Liu, K.; Xia, T.; Shi, Y.; Zhang, Q. Raman Scattering in the Transition-Metal Dichalcogenides of 1T′-$MoTe_2$,Td-$MoTe_2$, and Td-WTe_2. *Phys. Rev. B: Condens. Matter Mater. Phys.* **2016**, *94*, 214105.
(56) Dhakal, K. P.; Roy, S.; Jang, H.; Chen, X.; Yun, W. S.; Kim, H.; Lee, J. D.; Kim, J.; Ahn, J. H. Local Strain Induced Band Gap Modulation and Photoluminescence Enhancement of Multilayer Transition Metal Dichalcogenides. *Chem. Mater.* **2017**, *29*, 5124−5133.
(57) Kim, S.; Park, J.; Duong, D. L.; Cho, S.; Kim, S. W.; Yang, H. Proximity Engineering of the Van Der Waals Interaction in Multilayered Graphene. *ACS Appl. Mater. Interfaces* **2019**, *11*, 42528−42533.
(58) van der Zande, A. M.; Kunstmann, J.; Chernikov, A.; Chenet, D. A.; You, Y.-M.; Zhang, X. X.; Huang, P. Y.; Berkelbach, T. C.; Wang, L.; Zhang, F.; Hybertsen, M. S.; Muller, D. A.; Reichman, D. R.; Heinz, T. F.; Hone, J. C. Tailoring the Electronic Structure in Bilayer Molybdenum Disulfide *via* Interlayer Twist. *Nano Lett.* **2014**, *14*, 3869−3875.
(59) Giannozzi, P.; Andreussi, O.; Brumme, T.; Bunau, O.; Nardelli, M. B.; Calandra, M.; Car, R.; Cavazzoni, C.; Ceresoli, D.; Cococcioni, M.; Colonna, N.; Carnimeo, I.; Corso, A. D.; de-Gironcoli, S.; Delugas, P.; Distasio, R. A., Jr; Ferretti, A.; Floris, A.; Fratesi, G.; Fugallo, G.; et al. Advanced Capabilities for Materials Modeling with Quantum ESPRESSO. *J. Phys.: Condens. Matter* **2017**, *29*, 465901.
(60) Klimeš, J.; Bowler, D. R.; Michaelides, A. Van Der Waals Density Functionals Applied to Solids. *Phys. Rev. B: Condens. Matter Mater. Phys.* **2011**, *83*, 195131.

DOI: 10.1021/acsnano.9b08037
ACS Nano 2019, 13, 14437−14446

(61) Berland, K.; Cooper, V. R.; Lee, K.; Schröder, E.; Thonhauser, T.; Hyldgaard, P.; Lundqvist, B. Van Der Walls Forces in Density Functional Theory: a Review of the vdW-DF Method. *Rep. Prog. Phys.* **2015**, *78*, No. 066501.
(62) Thonhauser, T.; Zuluaga, S.; Arter, C. A.; Berland, K.; Schröder, E.; Hyldgaard, P. Spin Signature of Nonlocal Correlation Binding in Metal-Organic Frameworks. *Phys. Rev. Lett.* **2015**, *115*, 136402.

DOI: 10.1021/acsnano.9b08037
ACS Nano 2019, 13, 14437−14446